

Lithium Concentration and Atomic Chain Bridging Induced Strength–Ductility Synergy in Amorphous Lithiated Sulfur Cathodes

Yuan Gao^a, Siyi Huang^a, Xiaoyan Li^b, Yuli Chen^a, Bin Ding^{a,*}

^a National Key Laboratory of Strength and Structural Integrity, Institute of Solid Mechanics,
School of Aeronautic Science and Engineering, Beihang University, Beijing 100191, China

^b Center for Advanced Mechanics and Materials, Applied Mechanics Laboratory, Department of
Engineering Mechanics, Tsinghua University, Beijing 100084, China

* To whom correspondence may be addressed: bin_ding@buaa.edu.cn (Bin Ding)

This file contains:

Supplementary Figure 1-6

Supplementary Note

--Domain J -integral at the atomic scale

Supplementary Video 1-5

Supplementary Figure

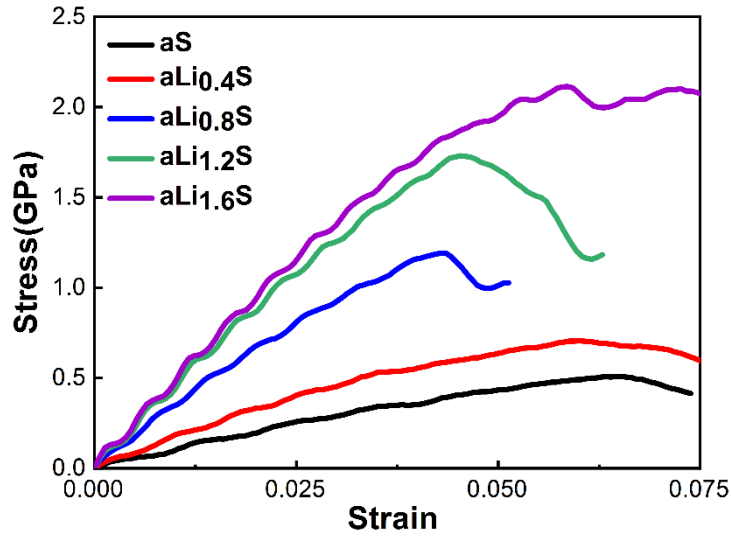


Fig. S1. Stress-Strain curves of a-Li_xS with a pre-existing edge crack under mode I loading at different Li concentrations ($0 \leq x \leq 1.6$). Distinct behaviors are identified to influence failure strain at lower lithium concentrations ($x \leq 0.4$) and higher lithium concentrations ($x > 0.4$) combined with an analysis of the relationship between crack tip distance and applied strain as depicted in Fig. 4b. At lower lithium concentrations ($x \leq 0.4$), crack initiation occurs early, followed by delayed rapid propagation, resulting in a large failure strain in the stress-strain curves. The resistance to crack propagation is ascribed to the presence of numerous atomic chains connecting the upper and lower crack surfaces. Conversely, at higher lithium concentrations ($x > 0.4$), the abundance of atomic chains diminishes significantly, and the strengthening and toughening effect of metallic lithium content begins to dominate. This leads to a transition to an increase in both peak stress and failure strain at higher lithium concentrations ($x > 0.4$).

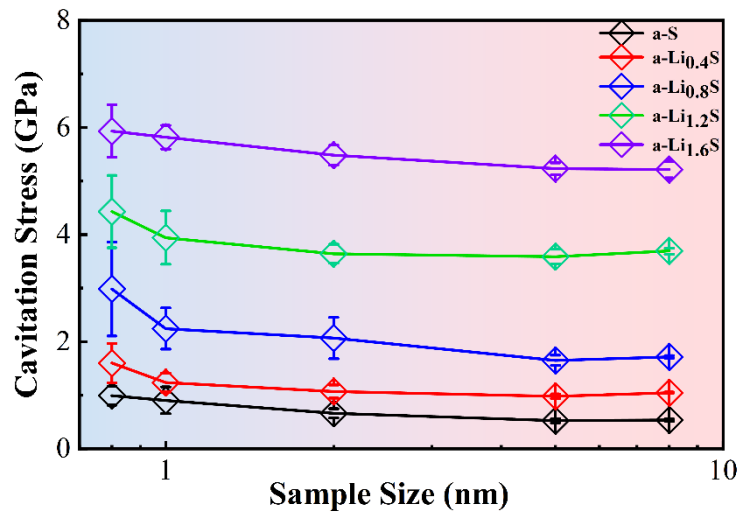


Fig. S2. Cavitation stress versus sample size for amorphous lithiated sulfur with varying lithium concentrations. Five sample sizes were adopted ranging from 0.8 nm to 8 nm for each specific lithium concentration. For each designated size, seven distinct cubic samples were randomly sliced from a 10 nm-sized cube. The error bar represents the standard deviation from statistical analyses for these seven independent samples. The upper and lower bounds of each curve are extracted to evaluate the spatial fluctuations of local hydrostatic stress of a-Li_xS in Fig. 2.

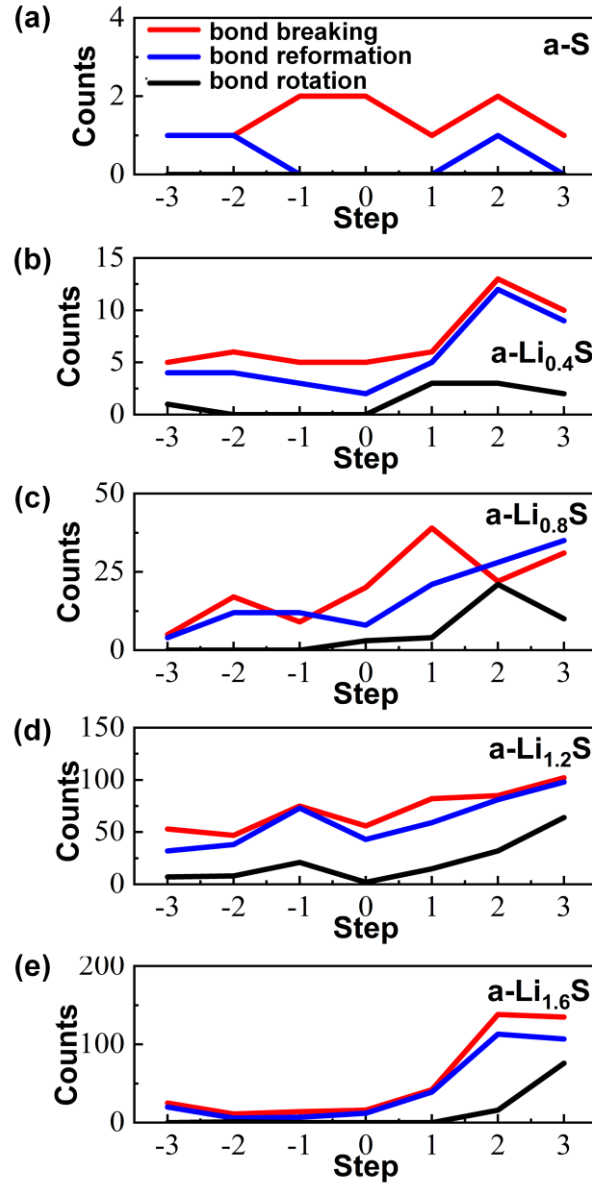


Fig. S3. Statistics of atomic bonding behavior of (a) a-S, (b) a-Li_{0.4}S, (c) a-Li_{0.8}S, (d) a-Li_{1.2}S, and (e) a-Li_{1.6}S. Step 0 is the moment at the onset of crack propagation. The figure shows the behavior of atomic bonds as breaking, rotating and reforming within the region of 2nm×2nm from the crack tip both before and after the initiation of crack propagation. In calculations, the critical distance for determining the breaking and reformation of atomic bonds are defined based on the first minimum in RDF. Specifically, these critical distances are identified as 2.6 Å for S-S bonds, 2.9 Å for Li-S bonds and 4.2 Å for Li-Li bonds, respectively. A bond is considered to undergo rotation when the vector direction rotation of two connected atomic bonds exceeds 30 degrees. Results indicate that at lower lithium concentrations, there are fewer bonding

dynamics at the crack tip. This is attributed to the higher proportion of S-S bonds, leading to changes in atomic bonding occurring in a discrete and abrupt manner. As the lithium concentration increases, the occurrence of dynamic bond behaviors rises significantly, accompanied by an increase in the proportion of reformations and rotations. This change provides an atomic scale explanation for the transition of a-Li_xS from brittle fracture to ductile fracture.

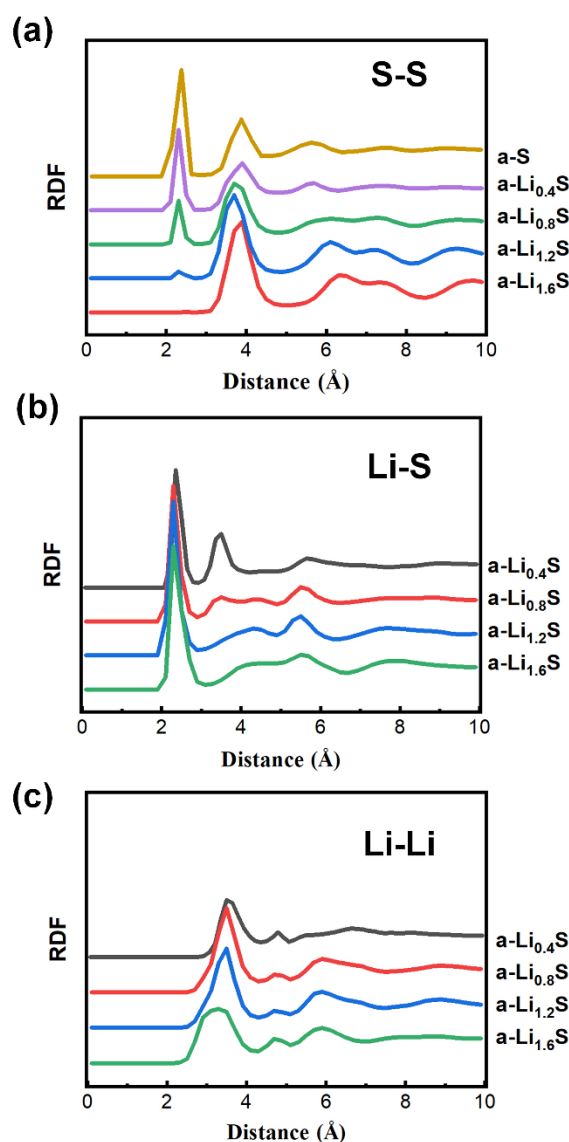


Fig. S4. Radial distribution functions for (a) S-S (b) Li-S, and (c) Li-Li in a-Li_xS at various lithium concentrations. (a) The first peak is attributed to the S-S covalent bond, while the second peak, located around 4.0 Å, is indicative of sulfur atoms

interconnected through Li. As lithium concentration increases, the intensity of the S–S first peak diminishes, signaling the disruption of S-S covalent bonds by the inserted Li; concurrently, the second peak intensifies, denoting an increase in Li-S bonds. (b) Across all compositions of $a\text{-Li}_x\text{S}$, the nearest neighbor peak of Li–S remains consistent, at approximately 2.3 Å. (c) As lithium concentration increase, Li–Li interactions intensify. Specifically, bond lengths contract from 3.5 Å to 3.1 Å, attributable to the formation of more Li-Li bonds in $a\text{-Li}_x\text{S}$.

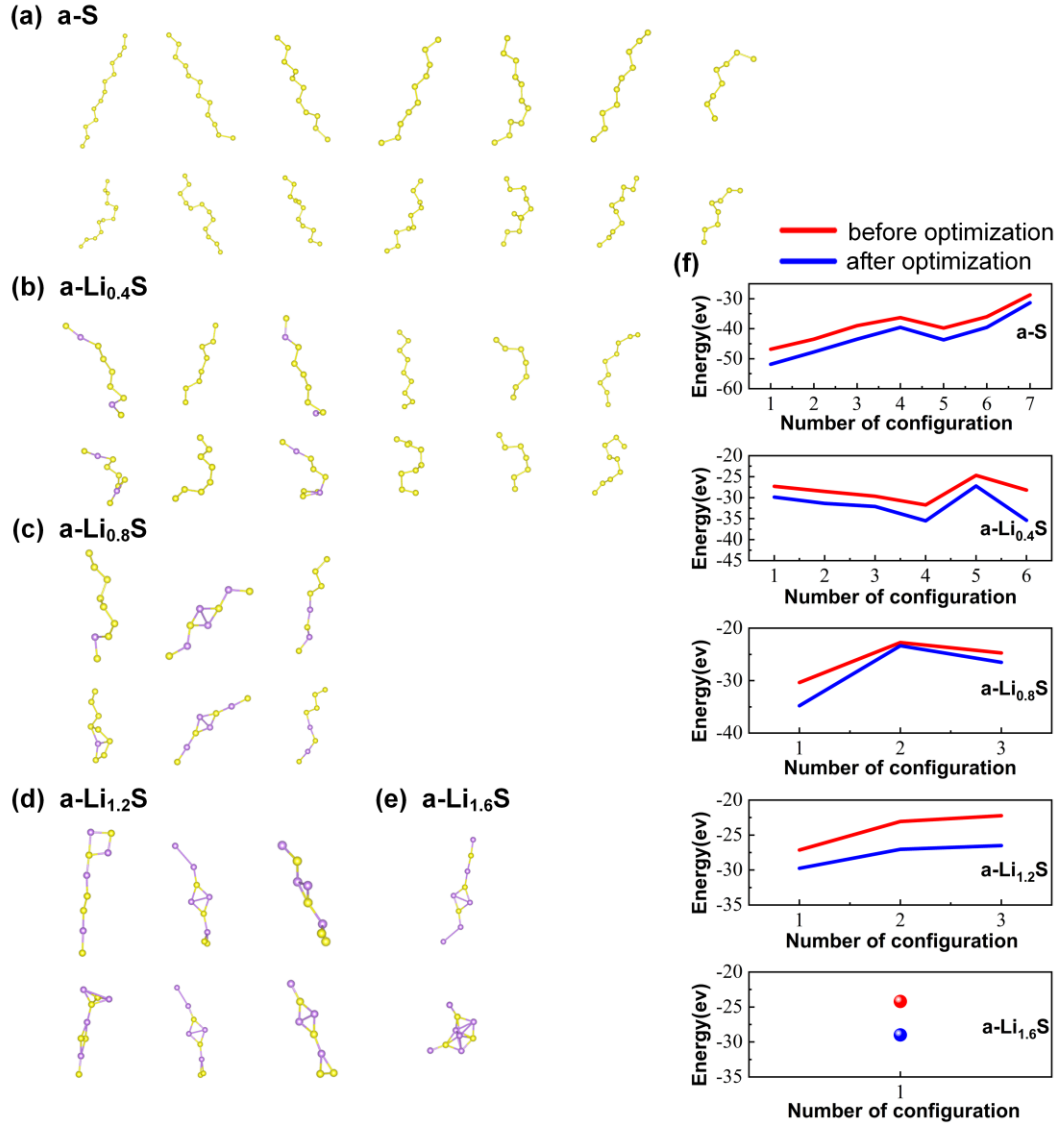


Fig. S5. Structure and energy of atomic chain configurations before and after optimization. Panels (a-e) represent atomic chains in (a) a-S, (b) a-Li_{0.4}S, (c) a-Li_{0.8}S, (d) a-Li_{1.2}S, and (e) a-Li_{1.6}S. The upper row represents configurations before optimization, while the lower row is the corresponding configurations after optimization. (f) Energy of atomic chain configuration before and after optimization. Sulfur and lithium atoms are colored by yellow and purple, respectively, in (a–e). The first principles calculations were performed using the Vienna ab initio simulation package (VASP)(Kresse and Furthmüller, 1996). We used the projector-augmented

wave (PAW) methods and the generalized gradient approximation of Perdew – Burke – Ernzerhof (GGA-PBE) for calculating the exchange–correlation functional. The energy cutoff on the wave function is taken as 350 eV and the Monkhorst–Pack scheme was used for the k-point sampling. In all calculations, the electronic energy convergence for a self-consistent loop and the force convergence for an atomic relaxation loop were set to 10⁻⁵eV and 0.02eV/Å, respectively.

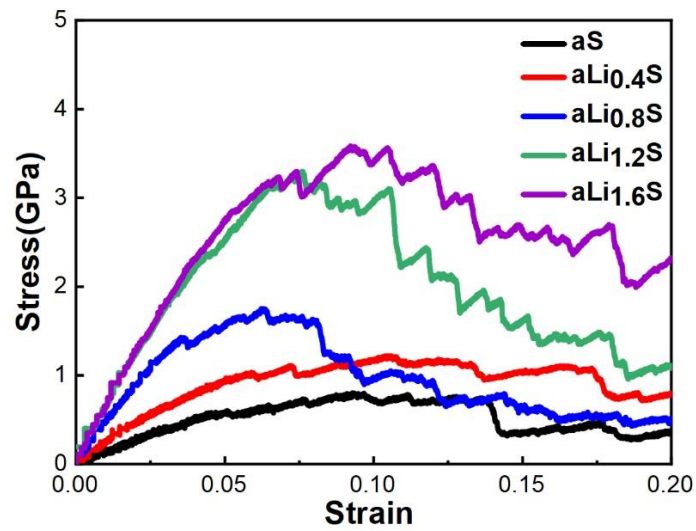
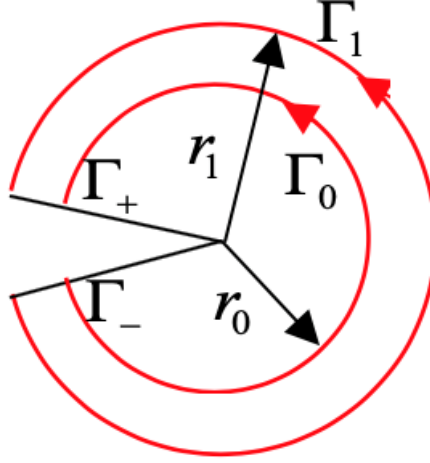


Fig. S6. Stress-Strain curves of a-Li_xS samples under uniaxial tensile loading at different Li concentrations ($0 \leq x \leq 1.6$). The samples dimensions are 4×7×2 nm³. During loading, periodic boundary condition was imposed in all three dimensions, and the temperature was maintained at 1K using NPT ensemble. The loading strain rate is 5×10⁸ s⁻¹.

Supplementary Note

Domain J -integral at the atomic scale:



For cracks, the J -integral is defined as (Jones and Zimmerman, 2010; Rice, 1968; Xie et al., 2023)

$$J = \int_{\Gamma} \left(w n_1 - \sigma_{ij} n_j \frac{\partial u_i}{\partial x_1} \right) d\Gamma \quad (1)$$

where the contour Γ starts at any point on the lower crack face and ends at any point on the upper crack face, w is the strain energy density, σ_{ij} and u_i denote components of stress and displacement, respectively, 1 is the direction parallel to the crack, and n_j is the unit vector outward normal to the contour Γ . Given the inherent discrete character of atomistic models in molecular dynamics simulations, contour integration cannot be applied directly. Therefore, this study utilized the atomic-scale equivalent domain J -integral approach. This method encompasses the ring-shaped domain around the crack tip with a closed contour. This contour consists of an inner circle Γ_0 with radius r_0 , an outer circle Γ_1 with radius r_1 and two crack faces. Subsequently, the domain integral formula can be derived as

$$J = \int_A \left[w \frac{dg}{dx_1} - \sigma_{ij} \frac{dg}{dx_i} \frac{\partial u_j}{\partial x_1} \right] dA \quad (2)$$

where g is the introduced auxiliary function taken as $g = (r - r_0) / (r_1 - r_0)$. We use an algorithm similar to finite element method to calculate the domain J -integral of a discrete MD sample, and equation (2) can be discretized as

$$J = \sum_{m=1}^M \left[\left(w^m - \sigma_{11}^m \frac{\partial u_1^m}{\partial x_1} - \sigma_{12}^m \frac{\partial u_2^m}{\partial x_1} \right) \frac{dg^m}{dx_1} - \left(\sigma_{21}^m \frac{\partial u_1^m}{\partial x_1} + \sigma_{22}^m \frac{\partial u_2^m}{\partial x_1} \right) \frac{dg^m}{dx_2} \right] dA^m \quad (3)$$

where M is the total number of elements within the integration region, superscript m presents the m_{th} element. When partitioning the domain, we refer to the finite element's four-node linear shape functions, divide the region with radius and angle instead of x_1 and x_2 coordinates. The area of each element can be given by:

$$dA^m = \frac{1}{2} \left[(r + dr)^2 - r^2 \right] d\theta \quad (4)$$

By calculating the difference in potential energy before and after deformation, the strain energy density of the m_{th} element can be obtained as

$$w^m = \left[\sum_{im=1}^{mm} (p^{im} - p_0^{im}) \right] / V^m \quad (5)$$

where mm is the total number of atoms within the m_{th} element, p^{im} and p_0^{im} are the atomic potential energies of atom im before and after deformation, respectively, V^m is the volume of the m_{th} element, which can be obtain by multiplied dA^m by the thickness of this quasi-3D system.

By averaging over all atoms within the region, the average stress within that region can be obtained:

$$\sigma_{kj}^m = \left(\sum_{im=1}^{mm} \sigma_{kj}^{im} \right) / V^m \quad (6)$$

where σ_{kj}^{in} is the kj stress component of atom i within the m_{th} element at the current time step.

A two-dimensional Gaussian integration, utilizing four integration points, is employed to compute the derivatives for each respective element. Initially, the displacements of the four nodes are calculated by averaging the displacements of nearby atoms. This average is taken within a 0.3 nm cutoff and is weighted according to atomic masses.

$$(u_1, u_2)_i = \frac{\sum_{\alpha=1}^N m^\alpha u_1^\alpha}{\sum_{\alpha=1}^N m^\alpha}, \frac{\sum_{\alpha=1}^N m^\alpha u_2^\alpha}{\sum_{\alpha=1}^N m^\alpha}, i = 1, \dots, 4 \quad (7)$$

where u_1^α, u_2^α represent the displacement of the atom α in the two directions, respectively and m^α is the mass of the atom α . The coordinates of atoms within each region are determined through interpolation using finite element shape functions.

$$x_j^m(\xi, \eta) = \sum_{i=1}^4 N_i(\xi, \eta) x_j^{im} \quad (8)$$

where x_j^{im} is the coordinate of node i in the j -direction within the m_{th} element. The shape function can be expressed as $N_i = 0.25(1 + \xi_i \xi)(1 + \eta_i \eta)$. Therefore, the ε_j and $g_{,j}$ of the m_{th} element can be calculated as

$$\begin{aligned} \varepsilon_j^m(\xi, \eta) &= \frac{\partial u_j}{\partial x_1} = \sum_{i=1}^4 (\partial N_i / \partial x_1) u_j^{im} \\ g_{,j}^m(\xi, \eta) &= \frac{\partial g}{\partial x_j} = \sum_{i=1}^4 (\partial N_i / \partial x_j) g^{im} \end{aligned} \quad (9)$$

In order to transform the integral interval from an area integral to a double integral, it is necessary to calculate the Jacobian determinant for each element:

$$J_{\text{Jacobian}}^m = \begin{bmatrix} \partial x_1 / \partial \xi & \partial x_2 / \partial \xi \\ \partial x_1 / \partial \eta & \partial x_2 / \partial \eta \end{bmatrix} \quad (10)$$

Finally, the m_{th} elemental displacement derivatives are

$$\begin{aligned}
\frac{\partial u_j^m}{\partial x_1} &= \frac{1}{A^m} \int_A \varepsilon_j^m dA = \frac{1}{A^m} \int_{-1}^1 \int_{-1}^1 \varepsilon_j^m |J_{\text{Jacobian}}^m| d\xi d\eta \\
&= \frac{1}{A^m} \sum_{k=1,2} \sum_{l=1,2} \varepsilon_j^m(\xi_k, \eta_l) |J_{\text{Jacobian}}^m(\xi_k, \eta_l)| H_k H_l \\
\frac{dg^m}{dx_j} &= \frac{1}{A^m} \sum_{k=1,2} \sum_{l=1,2} g_{,j}^m(\xi_k, \eta_l) |J_{\text{Jacobian}}^m(\xi_k, \eta_l)| H_k H_l \\
A^m &= \int_{A^m} dA = \sum_{k=1,2} \sum_{l=1,2} |J_{\text{Jacobian}}^m(\xi_k, \eta_l)| H_k H_l
\end{aligned} \tag{11}$$

where H_k and H_l are the weights at the Gaussian integration points, $H_k = H_l = 1$ here.

The domain J -integral value can be obtained by substituting the above equation (4-6)

and (11) into equation (3).

Table S1

J -integral values for each integral domain in a-Li_xS

x in a-Li _x S	Inner radius (Å)	Outer radius (Å)	J_{IC} (J/m ²)	Inner radius (Å)	Outer radius (Å)	J_{IC} (J/m ²)
0	50	90	0.5217	50	100	0.5110
0	50	110	0.4916	50	120	0.4822
0	60	90	0.4948	60	100	0.4881
0	60	110	0.4694	60	120	0.4622
0.4	50	90	0.8986	50	100	0.8843
0.4	50	110	0.8807	50	120	0.8989
0.4	60	90	0.9002	60	100	0.8819
0.4	60	110	0.8781	60	120	0.8997
0.8	50	90	1.5274	50	100	1.5409
0.8	50	110	1.5378	50	120	1.5338
0.8	60	90	1.5565	60	100	1.5661
0.8	60	110	1.5573	60	120	1.5494

1.2	50	90	2.9426	50	100	2.9929
1.2	50	110	2.9987	50	120	2.9980
1.2	60	90	2.9663	60	100	3.0232
1.2	60	110	3.0241	60	120	3.0191
1.6	50	90	3.0966	50	100	3.1475
1.6	50	110	3.1484	50	120	3.1624
1.6	60	90	3.1394	60	100	3.1923
1.6	60	110	3.1845	60	120	3.1947

Supplementary Video

Video S1. Crack propagation in a-S. As loading strain increases, nanosized voids spontaneously nucleate ahead of the crack tip, then gradually grow and, in time, coalesce with the main crack. The coalescence of these nanovoids results in accelerated crack propagation. Simultaneously, an increase in loading strain reveals a significant presence of atomic chains behind the crack tip, which acts crack bridging to resist crack face separation and crack propagation.

Video S2. Crack propagation in a-Li_{0.4}S. As loading strain increases, nanosized voids spontaneously nucleate ahead of the crack tip, then gradually grow and, in time, coalesce with the main crack. The coalescence of these nanovoids results in accelerated crack propagation. Simultaneously, an increase in loading strain reveals numerous presence of atomic chains behind the crack tip, which acts crack bridging to resist crack face separation and crack propagation. Due to the addition of lithium, the peak stress in

the stress-strain curve increases

Video S3. Crack propagation in a-Li_{0.8}S. As loading strain increases, nanosized voids spontaneously nucleate ahead of the crack tip, then gradually grow and coalesce with the main crack. The coalescence of these nanovoids results in crack propagation. In a-Li_{0.8}S, the atomic chains behind the crack tip become less prevalent, resulting in a decrease in the failure strain associated with the peak stress.

Video S4. Crack propagation in a-Li_{1.2}S. As loading strain increases, nanosized voids spontaneously nucleate ahead of the crack tip, then gradually grow and coalesce with the main crack. The coalescence of these nanovoids results in crack propagation. Few atomic chains are observed behind the crack tip, and the increase in loading strain is due to the increases of lithium concentration.

Video S5. Crack propagation in a-Li_{1.6}S. As loading strain increases, extensive shear bands launch around the crack tip. This sample undergoes significant plastic deformation, leading to expansive plastic zones near the crack tip. The launch of shear bands results in ductile fracture mode. Almost no atomic chains are observed behind the crack tip, and the increase in failure strain is purely due to the increases of lithium concentration.

References

- Jones, R.E., Zimmerman, J.A., 2010. The construction and application of an atomistic J-integral via Hardy estimates of continuum fields. *Journal of the Mechanics and Physics of Solids* 58, 1318-1337. <https://doi.org/10.1016/j.jmps.2010.06.001>
- Kresse, G., Furthmüller, J., 1996. Efficiency of ab-initio total energy calculations for metals and semiconductors using a plane-wave basis set. *Computational materials science* 6, 15-50. [https://doi.org/10.1016/0927-0256\(96\)00008-0](https://doi.org/10.1016/0927-0256(96)00008-0)
- Rice, J.R., 1968. A path independent integral and the approximate analysis of strain

concentration by notches and cracks. Journal of Applied Mechanics 35, 379-386.<https://doi.org/10.1115/1.3601206>

Xie, W., Zhang, X., Wei, Y., Gao, H., 2023. Toughening two dimensional materials through lattice disorder. Carbon, 118268.<https://doi.org/10.1016/j.carbon.2023.118268>